



Unravelling electrocatalytic concerted diatomic-ensembles over superior hydrogen-evolution array structured by NiMo/Mo₂N heteronanojunctions

Huanli Jia^{a,b}, Haiyan Wang^{a,*}, Fangfang Yan^{a,b}, Hucheng Zhang^{a,*}, Ze Li^a, Jianji Wang^{a,*}

^a Collaborative Innovation Centre of Henan Province for Green Manufacturing of Fine Chemicals, Key Laboratory of Green Chemical Media and Reactions, Ministry of Education, School of Chemistry and Chemical Engineering, Henan Normal University, Xinxiang, Henan 453007, PR China

^b College of Mechanical and Electrical Engineering, Xinxiang University, Xinxiang, Henan 453003, PR China

ARTICLE INFO

Keywords:

Hydrogen evolution reaction
Concerted diatomic electrocatalysis
Heteronanojunction array
Surface reconstruction
Ensemble effect

ABSTRACT

The concerted catalysis throughout multiple elementary steps is key to impel sluggish hydrogen evolution reaction (HER). Herein, NiMo/Mo₂N/NC(500-R) array is constructed by embedding densely packed NiMo/Mo₂N heterojunctions into nanorod skeleton of nitrogen-rich derived carbons (NC), then followed by electrochemical surface reconstruction. The great electrochemical surface area of resultant electrocatalyst implies fully-exposed concerted diatomic-ensembles. The ensemble effect of unique heteronanojunction induces charge polarizations between Mo and Ni species, gives pseudocapacitance comparable to supercapacitors, and pumps mass transfers to refresh entire HER process. The exceptional activity is demonstrated by ultra-low overpotentials of 5.8 and 200.6 mV respectively at 10 and 1000 mA cm⁻², the impressive durability is indicated by lasting alkaline HER for 1000 h at 1 A cm⁻². Moreover, the performances in water-alkali electrolyzer outperform most reported catalysts. This work presents valuable insights into concerted catalysis and designing efficient and durable electrocatalysts by ensemble effect from different metal heterojunctions for commercial applications.

1. Introduction

The escalation of environmental apprehensions has motivated immense interest in hydrogen energy that has high gravimetric energy density, ubiquitous availability on earth, and broad applications without pollutant emissions [1–4]. Currently, hydrogen evolution reaction (HER) from water, powered by clean electricity, is recognized as the most propitious technique of sustainable production. Nevertheless, the renewable supply from photovoltaics and wind energies fluctuates with spatial, temporal, climatic and seasonal factors. Consequently, the real-time conversion of these energies necessitates HER electrocatalysts that exhibit sensitive responses to dynamic input power, and proficient operations in wide current-density range and long-term durability [5–7].

Acidic HER usually progresses two to three orders of magnitude faster than alkaline media [8,9]. However, the vulnerability of metal-based catalysts and proton exchange membrane in acidic solutions results in preference for large-scale hydrogen production in alkaline media [10–12]. Therefrom, there are extensive explorations of low-cost transition metal-based catalysts to replace scarce noble metals and minimize HER barriers [13–20]. Despite these efforts,

sluggish kinetics on the electrocatalysts incurs high overpotentials, and becomes especially egregious at industrial current densities more than 500 mA cm⁻² [21,22].

An effective strategy has been developed by vertical growth of transition metal-based nanoarray on metal substrates, and the resultant monolithic catalysts are brought about smooth mass transfer channels and negligible interface electric-resistances, markedly improving catalytic efficiency [23–27]. Thus far, most reported nanoarrays tend to have high crystallinity with moderate specific surface areas, leading to unsatisfactory HER activity and long-term stability in large current densities [24,28–32]. While the arrays with nanostructured nanorods promises to impart catalysts with more exposed active sites and drive large current water splitting, these structures risk geometrical collapse during the preparation and catalytic processes, increasing charge and mass transfer barriers [33]. Hence, it is relentlessly pursued to develop arrays with nanostructured rods that offer high catalytic activity and robust tolerance in industrial water electrolysis.

Alkaline HER is launched from Volmer reaction ($\text{H}_2\text{O} + \text{e}^- \rightarrow \text{H}^* + \text{OH}^-$), and followed either by Heyrovsky ($\text{H}_2\text{O} + \text{e}^- + \text{H}^* \rightarrow \text{H}_2 + \text{OH}^-$) or Tafel reaction ($2 \text{H}^* \rightarrow \text{H}_2$) [34–37]. The rate of HER is chiefly governed by water dissociation and adsorption/desorption of intermediates (H^*

* Corresponding authors.

E-mail addresses: wanghaiyan@htu.edu.cn (H. Wang), hzhang@htu.edu.cn (H. Zhang), jwang@htu.edu.cn (J. Wang).

<https://doi.org/10.1016/j.apcatb.2023.123362>

Received 21 August 2023; Received in revised form 22 September 2023; Accepted 4 October 2023

Available online 5 October 2023

0926-3373/© 2023 Elsevier B.V. All rights reserved.

and OH^{*}). It is widely accepted that strong adsorption of H^{*}/OH^{*} can poison active sites by blocking water molecule re-adsorption and hydrogen recombination, thereby suggesting that the single active structure may not offer optimal catalytic efficiencies for all steps [10, 38]. To circumvent the sluggish multistep reactions, the quintessential HER electrocatalysts should be rationally designed with multiple components, each targeting the catalysis of designated elementary steps. A proficient strategy, as reported, generates distinct domains over electrocatalysts with defined bifunctionality: one domain for water dissociation and OH⁻ desorption, the other domain for H^{*} adsorption and successive H₂ production [39–41]. The dual effect lowers the kinetic barriers of individual elementary step more effectively on electrocatalysts than on single-functional ones. Despite significant advances in enhancing electrocatalysis, it remains challenging to fulfill high HER current for industrial applications, resulting from the well-separated domains with the limited sites of synergistical catalysis. Concerted diatomic-ensembles (CDAEs) with dense dual active sites can offer a solution by inducing synchronous catalysis in multistep reactions. However, this proposition holds true only if the electrocatalytic interfaces are engineered to provide asymmetrical charge distributions for favorable electronic structure and adequate spaces for CDAE accessibility.

Here, we report a novel nanostructured array, wherein the nanorods are constructed using nanosized NiMo/Mo₂N heterojunctions, delivering exceptionally high catalytic activity and durability in large-current alkaline HER. During the digestion-nitridation process of the ionic liquid (IL) of 1-ethyl-3-methylimidazolium tetrazolate ([C₂mim][Tet], Scheme S1), the metallic NiMo/Mo₂N was incorporated into nanorod skeletons of IL-derived carbons (NC) in the NiMo/Mo₂N/NC(500) array, and followed by the hydroxylation of Ni species through electrochemical surface reconstruction (ESRC) to harvest NiMo/Mo₂N/NC(500-R). The architecture of heteronanojunctions leads to an exceedingly large electrochemical surface area (ECSA) that is further augmented by ESRC. The catalyst demonstrates abundant CDAEs in NiMo/Mo₂N, and the asymmetrical charge distributions in Mo-Ni species. Resultantly, the fully exposed CDAEs provide arenas for multiple elementary steps, therein, Mo-Ni species trigger synergistical cleavage of H-OH, and are refreshed by facilitating OH^{*} desorption and H^{*}-involved elementary steps. Furthermore, the nitrogen-rich NC integrates NiMo/Mo₂N together to impart the 3D self-supported nanoarray with robust durability, efficient charge transfer and mass transport. Hence, the concerted catalysis alleviates blocking effect on water molecule re-adsorption and hydrogen recombination, thereby achieving superior kinetics in HER and water-alkali electrolyzer.

2. Experimental section

2.1. Growth of NiMoO₄·xH₂O cuboid arrays on Ni foam

The NiMoO₄·xH₂O nanoarray was synthesized by a hydrothermal route. Firstly, a piece of commercial Ni foam (1 cm × 3 cm) was ultrasonically cleaned in aqueous HCl solution of 3 mol L⁻¹ for 15 min to remove the surface oxides, and washed in turn with absolute ethanol and deionized water for several cycles, then dried in a vacuum furnace at 60 °C for 6 h. Next, the pretreated Ni foam was submerged vertically into the solution of 8 mL deionized water containing 0.12 mmol (NH₄)₆Mo₇O₂₄·4 H₂O and 0.48 mmol Ni(NO₃)₂·6 H₂O in a Teflon-lined stainless autoclave (15 mL). Lastly, the autoclave was sealed and heated at 150 °C for 6 h in an oven, and then cooled down to room temperature [42]. The as-grown cuboid arrays were washed with deionized water for several times and dried at 60 °C in vacuum, and denoted as NiMoO₄·xH₂O. For comparison, the NiMoO₄ cuboid arrays on Ni foam were obtained as the NiMoO₄·xH₂O was heated in N₂ flow at 500 °C for 2 h.

2.2. Synthesis of 1-ethyl-3-methylimidazolium tetrazolate

The [C₂mim][Tet] was synthesized from [C₂mim][Br] and tetrazole by the standard anion exchange procedures as reported in our previous work [43]. Typically, Ambersep 900(OH) resin was fully rinsed by deionized water, and filled compactly into a quartz chromatographic column of 3 cm diameter. Then, 1.5 wt% aqueous solution of [C₂mim][Br] was transfer to the resin column. After static incubation for OH⁻ exchange more than 8 h, and the aqueous solution of 1-ethyl-3-methylimidazolium hydroxide ([C₂mim][OH]) was collected from the effluent in one drop every three seconds. Finally, the equimolar amount of tetrazole was added to [C₂mim][OH] aqueous solution, and was stirred for 24 h. [C₂mim][Tet] was harvested by removing water through rotary evaporation at 50 °C.

2.3. Synthesis of NiMo/Mo₂N/NC

Generally, 100 mg [C₂mim][Tet] was spin-coated evenly on the as-prepared cuboid arrays with loading NiMoO₄·xH₂O in 32.2 mg cm⁻². Then, the sample was placed in a porcelain boat wrapped by copper foil, and heated to 500 °C at 10 °C min⁻¹ in N₂ flow. After calcination for 2 h, the tube furnace was naturally cooled to room temperature, the sample was washed in turn with deionized water and ethanol for several times and dried at 60 °C. The as-obtained nanoarray was denoted as NiMo/Mo₂N/NC(500). Following the same synthetic processes, Ni₃Mo₃N/NC(600) and Mo₂C/NC(700) were respectively prepared at the calcination temperatures of 600 and 700 °C.

Additionally, the control samples of NiMo/Mo₂N/NC(500) were respectively prepared with the different [C₂mim][Tet] loadings of 25, 50, and 200 mg at the calcination temperature of 500 °C. For comparison, NiMoO₄·xH₂O powder was blended with [C₂mim][Tet] in the same mass ratio as that for NiMoO₄·xH₂O, and the mixture was calcined at 500, 600, and 700 °C to synthesize the powder samples of NiMo/Mo₂N/NC(500), Ni₃Mo₃N/NC(600), and Mo₂C/NC(700), respectively.

2.4. Synthesis of NiFe-LDH/NiMo/Mo₂N/NC(500)

The electrodeposition was employed to grow NiFe-layered double hydroxide (NiFe-LDH) using NiMo/Mo₂N/NC(500) as the substrate. When the electrodeposition is operated in a three-electrode configuration, NiMo/Mo₂N/NC(500) was directly used as the working electrode, a graphite rod as the counter electrode, and an Ag/AgCl electrode as the reference electrode. The electrolyte is an aqueous solution containing 0.15 M Ni(NO₃)₂·6 H₂O and 0.15 M FeSO₄·7 H₂O. Given a constant potential at -1.0 V vs. Ag/AgCl, the electrodeposition was implemented for 300 s, and the as-obtained electrocatalyst was denoted as NiFe-LDH/NiMo/Mo₂N/NC(500). As comparison, NiFe-LDH was produced by the same way as Ni foam was used as the working electrode.

2.5. Electrochemical measurement

All electrochemical measurements were performed on a CHI660E electrochemical workstation (Chenhua Instruments Co. Ltd.) with a standard three-electrode setup in N₂-saturated (HER) or O₂-saturated (OER) 1 M KOH aqueous solution at room temperature. Therein, the electrocatalyst on Ni foam was directly employed as working electrode, an Ag/AgCl electrode (Ag/AgCl in a saturated KCl solution) as reference electrode, and a graphite rod as counter electrodes. To achieve test reliability, the working electrode was sealed with epoxy prior to measurements, ensuring that the exact geometric area immersed in the electrolyte is 0.5 cm × 1 cm. The reference electrode was calibrated against the reversible hydrogen electrode following standard procedures. In the control experimental, commercial 20 wt% Pt/C or RuO₂ was well-dispersed in a diluted Nafion solution containing of 500 μL ethanol, 450 μL water, and 50 μL Nafion to form a homogeneous suspension, then, the above homogeneous suspension of 5 μL was cast on Ni foam

with a metal loading of 2 mg cm^{-2} .

The activity of catalysts in electrocatalytic HER (or OER) was evaluated via linear sweep voltammetry (LSV) curves at a sweep rate of 2 mV s^{-1} with 90% iR-compensation for the data. To eliminate the double layer current, the back scans were selected for linear sweep voltammetry. To evaluate long-term stability, chronopotentiometry was conducted at the current density of 1000 mA cm^{-2} for HER and 500 mA cm^{-2} for OER. All the potentials were calibrated reference to reversible hydrogen electrode (RHE) by the equation $E(\text{RHE}) = E(\text{Ag}/\text{AgCl}) + 0.198 \text{ V} + 0.059 \text{ V} \cdot \text{pH}$, and the current densities (j) were normalized by the geometrical surface area unless otherwise mentioned. All tests were repeated at least three times to ensure the data reliability.

For the two-electrode water electrolysis, the as-prepared NiFe-LDH/NiMo/Mo₂N/NC(500) or NiMo/Mo₂N/NC(500-R) was used as the anode, and NiMo/Mo₂N/NC(500-R), NiMo/Mo₂N/NC(500) or NiFe-LDH/NiMo/Mo₂N/NC(500) as the cathode. The polarization curves were measured at a sweep rate of 2 mV s^{-1} in 1 M KOH at room temperature, and stability test was carried out under constant current

densities of 500 mA cm^{-2} .

3. Results and discussion

3.1. Microstructural features and surface hydroxylation

The nanostructured NiMo/Mo₂N/NC(500-R) was synthesized via nitridation-digestion of IL, and followed by ESRC (Fig. 1A). NiMoO₄·xH₂O nanorods were arranged in a cuboid-array with smooth surfaces and an average radial size of $0.54 \mu\text{m}$ as depicted in scanning electron microscopy (SEM) images (Fig. S1). Following a uniform coating of IL aqueous solution on the hydrophilic array surfaces, the thermal nitridation-digestion at 500°C converted NiMoO₄·xH₂O to NiMo/Mo₂N/NC(500). The conversion doesn't alter the array morphology, but splits the nanorods into slenderer ones with an average radial size of $0.18 \mu\text{m}$ (Fig. 1B and Fig. S2). Subsequently, NiMo/Mo₂N/NC(500-R) was activated via ESRC with 100 circles of cyclic voltammetry (CV) between 1.4~0.4 V vs. RHE in 1 M KOH, which led to

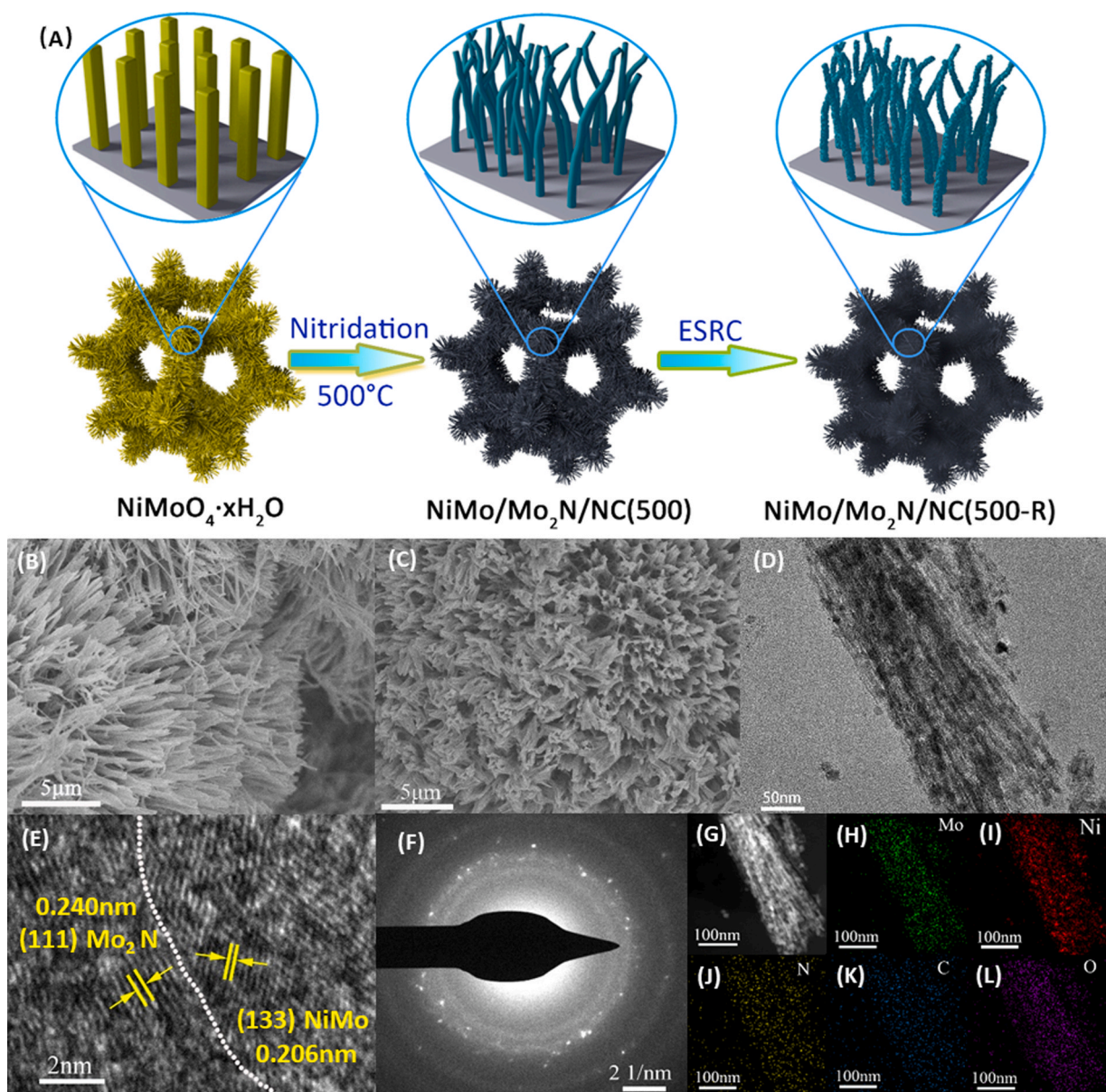


Fig. 1. Microscopic structures of NiMo/Mo₂N/NC(500-R). (A) Illustrating catalyst synthesis; SEM images of NiMo/Mo₂N/NC(500) before (B) and after (C) ESRC; (D) STEM image of single nanorod; (E) high-resolution TEM image; (F) SAED patterns; (G) HAADF-STEM image; (H)~(L) EDS mapping images for elements of Mo, Ni, N, C, and O.

slightly indistinct appearances due to surface hydroxylation (Fig. 1C) [44].

The scanning transmission electron microscopy (STEM) image depicted that the nanorods in NiMo/Mo₂N/NC(500-R) were constituted by tightly packed nanoparticles (Fig. 1D), rendering the diatomic-ensembles of Ni-Mo specie with fully expanded ECSA in electrocatalyst. NiMo-Mo₂N heterojunction is identified by white dot line in high-resolution TEM image, in which the lattice spaces of 0.240 and 0.206 nm are respectively indexed to (111) and (133) planes of Mo₂N and.

NiMo (Fig. 1E). The ring patterns with discrete dots in selected electron area diffraction (SAED) confirmed high dispersity of the nanoparticles (Fig. 1F). Moreover, the angle annular dark field (HAADF)-STEM image and energy dispersive X-ray spectroscopy (EDS) mapping images verified the extensive distributions of coupled Mo-Ni species over the nanorod (Fig. 1G~L).

With the exception of incomplete conversion of NiMoO₄·xH₂O at 400 °C (Fig. S3), Ni₃Mo₃N/NC(600) and Mo₂C/NC(700) nanoarrays were synthesized respectively at 600 and 700 °C, following similar procedures as outlined in Fig. 1A. Along with the analyses of their respective powders without interference from nickel foam (Fig. S4), X-ray diffraction (XRD) patterns suggested that NiMo/Mo₂N/NC(500) was composed of NiMo and Mo₂N in (Fig. 2A), Ni₃Mo₃N/NC(600) of Ni₃Mo₃N, and Mo₂C/NC(700) of Ni₃Mo₃N and β-Mo₂C (Fig. S5). After experiencing ESRC, the XRD patterns are unaltered in NiMo/Mo₂N/NC(500-R) and Ni₃Mo₃N/NC(600-R), whereas the Ni₃Mo₃N diffractions disappear in Mo₂C/NC(700-R). The disintegration of crystalline Ni₃Mo₃N during ESRC is verified by the blurrier appearances of Mo₂C/NC(700-R) as compared to the other samples (Fig. S6).

The highly dispersed crystallites in NiMo/Mo₂N/NC(500-R),

consistent with SAED result, were suggested by the most.

widened diffraction profiles, and their sizes were estimated using full width of half maximum (FWHM) of facet diffraction. Before and after ESRC, the crystallite size remained nearly constant for Mo₂N (3.14 nm), and decreased slightly from 10.70 to 10.33 nm for NiMo owing to surface hydroxylation in NiMo/Mo₂N/NC(500-R) (Fig. S7, Table S1). In contrast, the well-crystallized Ni₃Mo₃N/NC(600-R) exhibited a larger size of 23.32 nm for Ni₃Mo₃N. In the Raman spectra, moreover, the absence of bending (344.9 cm⁻¹) and stretching (940.8 cm⁻¹) vibrations of Mo-O^{45,46} provided additional proof of NiMoO₄·xH₂O conversions (Fig. 2B, Fig. S8), and the D and G bands clearly signaled the presence of IL-derived carbons [47]. Evidently, the self-supporting nanorods in NiMo/Mo₂N/NC(500-R) were integrated by NC with the nanosized NiMo-Mo₂N heterojunctions together.

The surface hydroxylation from ESRC makes OH species become more dominant in high-resolution X-ray photoelectron spectroscopy (XPS) of O 1s for these electrocatalysts (Fig. S9) [48,49]. The most antioxidative ability of NiMo/Mo₂N/NC(500-R), as indicated by thermogravimetric analysis in air, implies that surface hydroxylation defends fully exposed CDAEs from O₂ oxidation to a larger extent (Fig. S10). In linear sweep voltammetry (LSV) for oxygen evolution reaction (OER), the oxidation peak of Ni²⁺(Ni(OH)_{2-x})/Ni³⁺(NiOOH) indicates the occurrence of surface-hydroxylated Ni specie in Ni-based catalysts [50,51]. The anodic potential at 10 mA cm⁻² increases from 1.317 V for NiMo/Mo₂N/NC(500) to 1.349 V for NiMo/Mo₂N/NC(500-R) (Fig. 2C), implying that electrooxidation is deactivated by ESRC. Comparatively, the oxidation potential of Ni²⁺ in Ni₃Mo₃N/NC(600-R) is 21 mV higher than in Ni₃Mo₃N/NC(600), and is virtually unchanged in Mo₂C/NC(700) and Mo₂C/NC(700-R) (Fig. S11). Hence, the surfaces of NiMo/Mo₂N/NC(500-R) are profoundly hydroxylated by

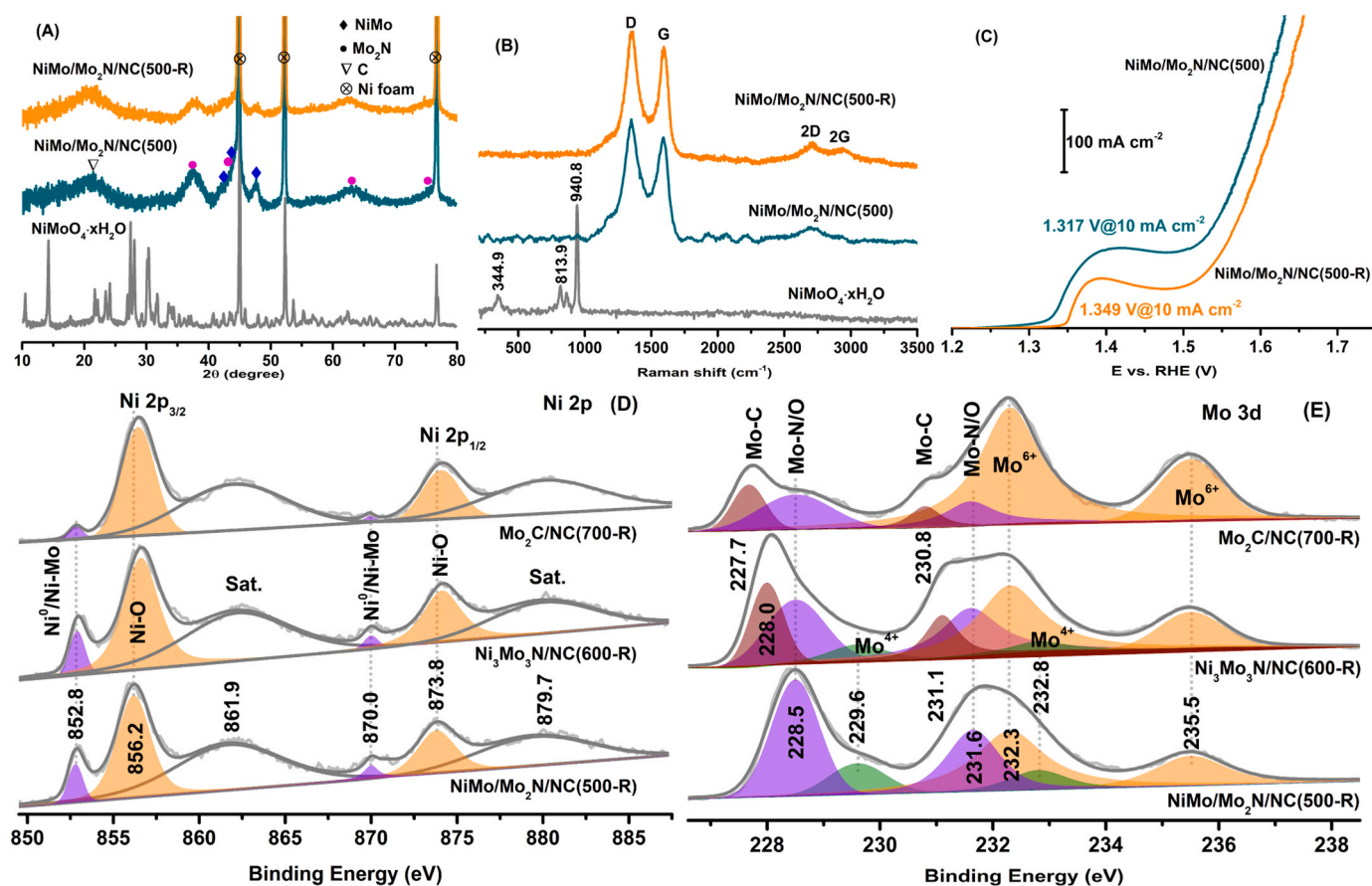


Fig. 2. Analyzing chemical components and hydroxylation in the electrocatalysts. (A) XRD patterns; (B) Raman spectra, (C) OER polarization curves at a scan rate of 2 mV s⁻¹ in 1 M KOH solution; and high-resolution XPS profiles of Ni 2p (D) and Mo 3d (E).

ESRC, $\text{Ni}_3\text{Mo}_3\text{N}/\text{NC}(600\text{-R})$ moderately, and $\text{Mo}_2\text{C}/\text{NC}(700\text{-R})$ weakly.

As active Ni-Mo species in CDAEs, XPS reveals that their favorable surface chemistry for HER is acquired by ESRC. The peaks at 852.8, 856.2, and 861.9 eV in $\text{Ni } 2p_{3/2}$ high-resolution XPS are respectively assigned to $\text{Ni}^0/\text{Ni-Mo}$ [42,46], Ni-O, and the relevant satellite peaks (Sat.) in $\text{NiMo}/\text{Mo}_2\text{N}/\text{NC}(500)$ (Fig. 2D) [45,52,53]. By comparison, the disintegration of crystalline $\text{Ni}_3\text{Mo}_3\text{N}$ in $\text{Mo}_2\text{C}/\text{NC}(700\text{-R})$, consistent with XRD result, is confirmed by the nearly disappeared peak of $\text{Ni}^0/\text{Ni-Mo}$, suggesting that hydroxylation considerably disrupts the chemical bonding of Ni with Mo atoms. Notably, these catalysts display identical binding energy of $\text{Ni}^0/\text{Ni-Mo}$, but the binding energy of Ni-O in

$\text{NiMo}/\text{Mo}_2\text{N}/\text{NC}(500\text{-R})$ are 0.3 eV lower than in $\text{Ni}_3\text{Mo}_3\text{N}/\text{NC}(600\text{-R})$ and $\text{Mo}_2\text{C}/\text{NC}(700\text{-R})$, making it more nucleophilic to serve as hydrogen acceptor. The deconvoluted triple peaks of $\text{Mo } 3d_{5/2}$ at 228.5, 229.6, and 232.3 eV are respectively attributed to Mo-N/O, Mo^{4+} , and Mo^{6+} in $\text{NiMo}/\text{Mo}_2\text{N}/\text{NC}(500\text{-R})$, therein, Mo^{4+} and Mo^{6+} suggest that Mo species in catalyst surfaces are easily oxidized by air upon transfer to measurement chamber (Fig. 2E) [52,54]. For Mo-N/O species in $\text{NiMo}/\text{Mo}_2\text{N}/\text{NC}(500\text{-R})$, the binding energy is 0.5 and 0.8 eV higher respectively than Mo-C species in $\text{Ni}_3\text{Mo}_3\text{N}/\text{NC}(600\text{-R})$ and $\text{Mo}_2\text{C}/\text{NC}(700\text{-R})$. Thus, $\text{NiMo}/\text{Mo}_2\text{N}/\text{NC}(500\text{-R})$, with partially oxidized Mo species but without Mo-C species, are more electrophilic to adsorb water

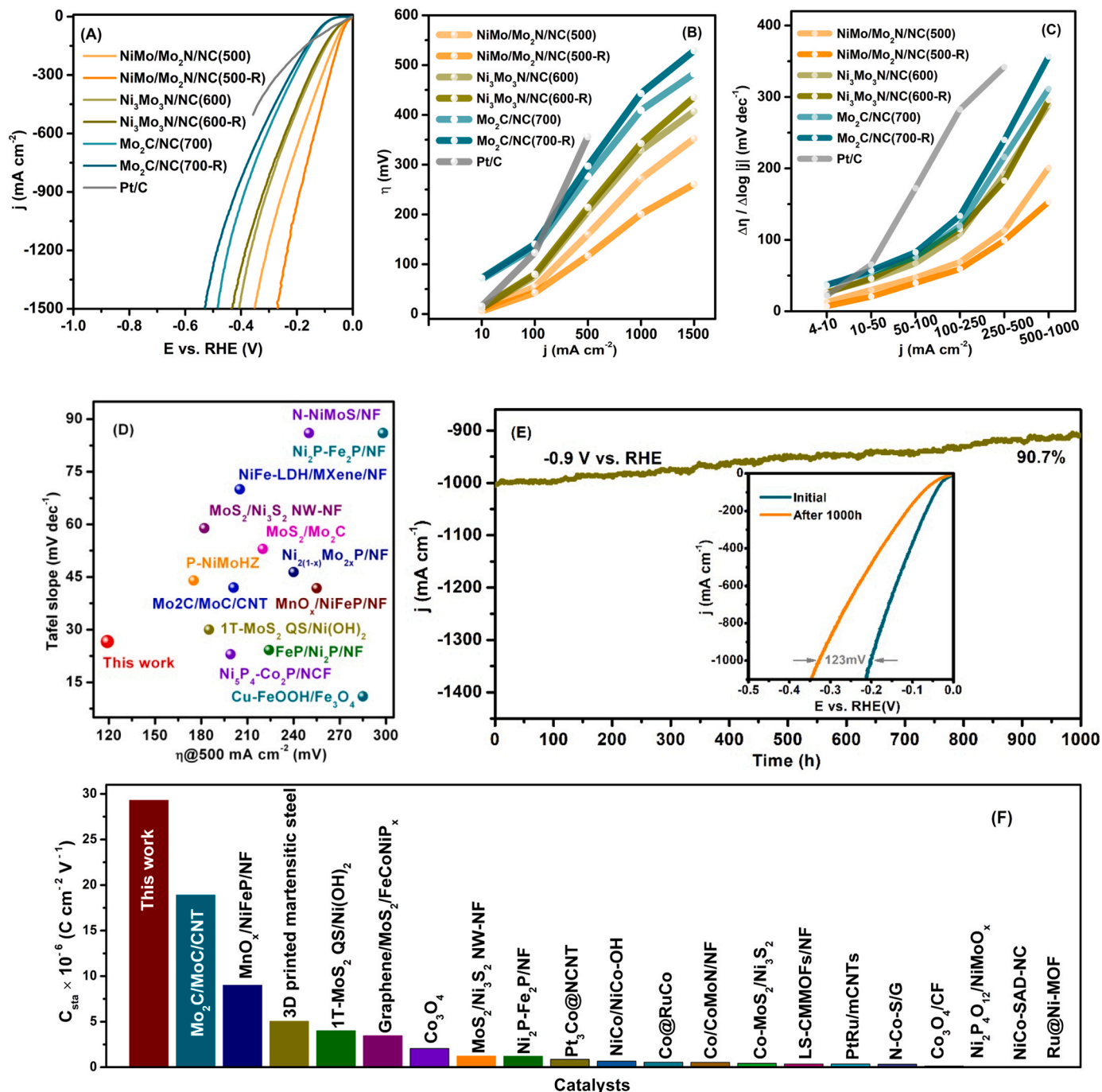


Fig. 3. Catalytic HER performances of the nanoarrays in 1 M KOH aqueous solution at room temperature. (A) 90% iR-compensation LSVs at a scan rate of 2 mV s⁻¹; (B) Overpotentials at different current densities; (C) $\Delta\eta/\Delta\log|j|$ in different current-density ranges; (D) Comparison of overpotential at 500 mA cm⁻² and Tafel slope of $\text{NiMo}/\text{Mo}_2\text{N}/\text{NC}(500\text{-R})$ with transition metal-based electrocatalysts; (E) Long-term stability of $\text{NiMo}/\text{Mo}_2\text{N}/\text{NC}(500\text{-R})$ at 1000 mA cm⁻², inset: LSV curves before and after stability test; (F) Comparison of long-term stability of $\text{NiMo}/\text{Mo}_2\text{N}/\text{NC}(500\text{-R})$ with the reported HER electrocatalysts.

readily.

All the experimental data collectively suggest that the nanorods in NiMo/Mo₂N/NC(500-R) are built from the heteronanojunctions between NiMo and NC-supporting Mo₂N, and the diatomic ensembles are derived from the chemical coupling of the surface-hydroxylated Ni species with the partially oxidized Mo species. Given that Ni₃Mo₃N is considered as chemical combination of Ni₂Mo₂ and NiMoN, [55] it's reasonable to propose that CDAEs are most abundant on the nanosized NiMo/Mo₂N/NC(500-R), moderate on the well-crystallized Ni₃Mo₃N/NC(600-R), and nearly absent on Mo₂C/NC(700-R) without Ni-Mo bonding.

3.2. Electrocatalysis in alkaline hydrogen evolution

The activities of electrocatalytic HER are evaluated by LSVs with 90% iR-compensation in 1 M KOH, with commercial Pt/C used for comparison (Fig. 3A). The overpotential (η) reflects the response of electrocatalysts to alkaline HER at a given current density (j) (Fig. 3B). For NiMo/Mo₂N/NC(500), η_{10} , η_{500} , η_{1000} , and η_{1500} at 10, 500, 1000, and 1500 mA cm⁻² respectively are 10.0, 159.7, 271.6, and 352.2 mV, substantially lower than those of the benchmark Pt/C catalyst. ESRC enhances catalytic activity, and reduces η_{10} , η_{500} , η_{1000} , and η_{1500} to 5.8, 117.0, 200.6, and 260.6 mV, respectively. Furthermore, $\Delta\eta/\Delta\log|j|$ ratios aptly address catalytic efficiencies over wide range of current density (Fig. 3C and Fig. S12) [45,56]. The $\Delta\eta/\Delta\log|j|$ of commercial Pt/C represents a sharp increase with current density. Besides the ultra-low η , $\Delta\eta/\Delta\log|j|$ ratios over the current density range of 4–10, 250–500, and 500–1000 mA cm⁻² respectively are as low as 12.9, 113.0, and 201.0 mV dec⁻¹ in NiMo/Mo₂N/NC(500), and are further lowered by ESRC to 7.0, 99.0, and 153.1 mV dec⁻¹ in NiMo/Mo₂N/NC(500-R). Compared with Ni₃Mo₃N/NC(600) and Mo₂C/NC(700), they exhibit larger η and $\Delta\eta/\Delta\log|j|$ than NiMo/Mo₂N/NC(500). With ESRC, η and $\Delta\eta/\Delta\log|j|$ increase in Mo₂C/NC(700-R) but retain largely unchanged in Ni₃Mo₃N/NC(600-R). Evidently, the decomposition of Ni₃Mo₃N in Mo₂C/NC(700-R) leads to in the absence of CDAEs and conducts the most sluggish kinetics, which becomes more noticeable as the current densities increase. It's the nanosized NiMo/Mo₂N heterojunctions in NiMo/Mo₂N/NC(500-R) that has the richest CDAEs to catalyze HER, sensitively responds to tiny current densities, and deliver exceptional catalytic efficiency even at industrial current densities exceeding 500 mA cm⁻².

Kinetically, Tafel slopes are direct parameter reflecting HER mechanism [57]. Tafel slopes of NiMo/Mo₂N/NC(500) and NiMo/Mo₂N/NC(500-R) are 34.52 and 26.63 mV dec⁻¹, close to theoretical values of 39.4 and 29.6 mV dec⁻¹ in Heyrovsky and Tafel steps, respectively (Fig. S13). Apparently, the rate-determining step (RDS) is Tafel and Heyrovsky reactions on NiMo/Mo₂N/NC(500), and is Tafel reaction on NiMo/Mo₂N/NC(500-R) that is typically identified as RDS from noble metal-based electrocatalysts in acidic HER [58]. In the absence of Ni-Mo species, Tafel slope of 65.40 mV dec⁻¹ suggests Volmer step to be RDS on Mo₂C/NC(700-R). Intrinsically, Tafel reaction as RDS in alkaline HER implies that HER rate relies mainly on H⁺-involved elementary steps. In this respect, NiMo/Mo₂N/NC(500-R) with surface-hydroxylated CDAEs catalyzes water dissociation more efficiently than NiMo/Mo₂N/NC(500), and far more than Mo₂C/NC(700-R). Compared with other state-of-the-art transition metal-based electrocatalysts, NiMo/Mo₂N/NC(500-R) performs most active in alkaline HER (Fig. 3D and Table S3).

The stability is a key criterion for commercial feasibility of NiMo/Mo₂N/NC(500-R), especially at large current densities [59]. After running the CV continuously for 10,000 cycles, the negligible change from LSVs suggests high cyclability.

of NiMo/Mo₂N/NC(500-R) (Fig. S14). As subjected to the chronoamperometry for testing long-term stability, NiMo/Mo₂N/NC(500-R) is run at 1000 mA cm⁻² for 1000 h, and the LSVs show an overpotential increase of only 123 mV (Fig. 3E). To evaluate catalyst stability quantitatively, the index of C_{sta} is introduced following the equation: [60]

$C_{sta} = j \cdot t \cdot \Delta E^{-1}$, where t is whole working time, and ΔE is overpotential difference after and before the test. NiMo/Mo₂N/NC(500-R) yields C_{sta} of 2.93×10^7 C cm⁻² V⁻¹, and surpasses the state-of-the-art HER catalysts (Fig. 3F and Table S4). After the chronoamperometry, the unchanged structure and composition of nanoarray show the strong mechanical and chemical stabilities of NiMo/Mo₂N/NC(500-R) in withstanding the massive release of H₂ bubbles (Fig. S15 and 16). It is NiMo-Mo₂N heteronanojunctions that are closely integrated by the nitrogen-rich derived-carbon to impart NiMo/Mo₂N/NC(500-R) with robust flexibility, enabling it to tolerate large operating current densities. Moreover, the Faradaic efficiencies on NiMo/Mo₂N/NC(500-R) were measured to be 99.93% and 98.47% respectively at 100 and 500 mA cm⁻² (Fig. S17), close to theoretical value, indicating almost complete charge utilization with negligible parasitic-side reactions in H₂ production [46,61].

3.3. Catalytic mechanism of CDAEs

NiMo/Mo₂N/NC(500-R) demonstrates the exceptionally large ECSA, addressing the contributions of low steric hindrances and abundant accessible CDAEs to intrinsic activity. As determined by double-layer capacitance (C_{dl}) (Fig. S18-S19), [31,62] ECSA of NiMo/Mo₂N/NC(500) is 654.7 times larger than nickel foam (Fig. 4A), and is extended by 42.0% in NiMo/Mo₂N/NC(500-R) owing to surface hydroxylation. Instead, ESRC reduces ECSAs by 1.1% and 8.4% respectively in Ni₃Mo₃N/NC(600-R) and Mo₂C/NC(700-R). These results are consistent with the surface hydroxylation to enhance NiMo/Mo₂N/NC(500-R) catalysis, but to deactivate Ni₃Mo₃N/NC(600-R) and Mo₂C/NC(700-R) in HER (Fig. 3B). According to ECSA and metal loadings from analysis of inductively coupled plasma mass spectrometry (Table S2), apparently, CDAEs in NiMo/Mo₂N/NC(500-R) are separated up to 4.0 and 9.5 folds more disperse than those in Ni₃Mo₃N/NC(600-R) and Mo₂C/NC(700-R), respectively. The better spaced CDAEs lend larger rooms to perform water and intermediate adsorption/desorption, and bring higher catalytic efficiencies as reflected by the exchange current density (j_0). [63] NiMo/Mo₂N/NC(500) gives j_0 of 7.56 mA cm⁻², is comparable with Ni₃Mo₃N/NC(600) (6.31 mA cm⁻²), and prominent to Mo₂C/NC(700) (1.01 mA cm⁻²) (Fig. S20). Correspondingly, ESRC increases j_0 with 34.8% in NiMo/Mo₂N/NC(500-R), but decreases j_0 with 4.5% and 41.6% respectively in Ni₃Mo₃N/NC(600-R) and Mo₂C/NC(700-R).

CDAEs adsorb strongly to bring about the charge redistributions among H⁺-O²⁻-H molecules, and the resultant water pre-decomposition leads to significant pseudocapacitance (C_{pseudo}) on NiMo/Mo₂N/NC(500-R) as revealed by pulse voltammetry [64,65]. The current responses in the pulse voltammetry protocols at different applied potentials (E) behave as a capacitor owing to the accumulated charge (Q) (Fig. S21). To avert bond rupture and formation, the linear fitting of Q against E is implemented in the potential region of 60–10 mV without HER current (Fig. S22), and the capacitance is obtained from the slope to be 8288.7 mF cm⁻² for NiMo/Mo₂N/NC(500) and 9741.0 mF cm⁻² for NiMo/Mo₂N/NC(500-R). C_{pseudo} is calculated by subtracting C_{dl} from the capacitance, and is 7443.7 mF cm⁻² for NiMo/Mo₂N/NC(500) and 8541.5 mF cm⁻² for NiMo/Mo₂N/NC(500-R) (Fig. 4B). After ESRC, the hydroxylation further enhances C_{pseudo} with ΔC_{pseudo} (1097.8 mF cm⁻²) that is 3 times larger than ΔC_{dl} (355.0 mF cm⁻²). Moreover, the reaction order (α) for NiMo/Mo₂N/NC(500-R) (5.10) is more than that for NiMo/Mo₂N/NC(500) (4.21) from the slope of $\log j$ versus $\log Q$ (Fig. 4B, Fig. S23), indicating the hydroxylation to promote reaction rate through charge accumulations. Because no significant redox peak is detected from the CV curves (Fig. S24), evidently, water pre-decomposition on CDAEs is the main contributor to C_{pseudo} , and yields C_{pseudo} comparable to plain supercapacitors. The heavier accumulated charge can trigger the speedier kinetics of water decomposition in NiMo/Mo₂N/NC(500-R), and gives larger HER current at a given overpotential.

Operando electrochemical impedance spectroscopy (EIS) unveiled the influence of mass transfers on catalytic kinetics in NiMo/Mo₂N/NC

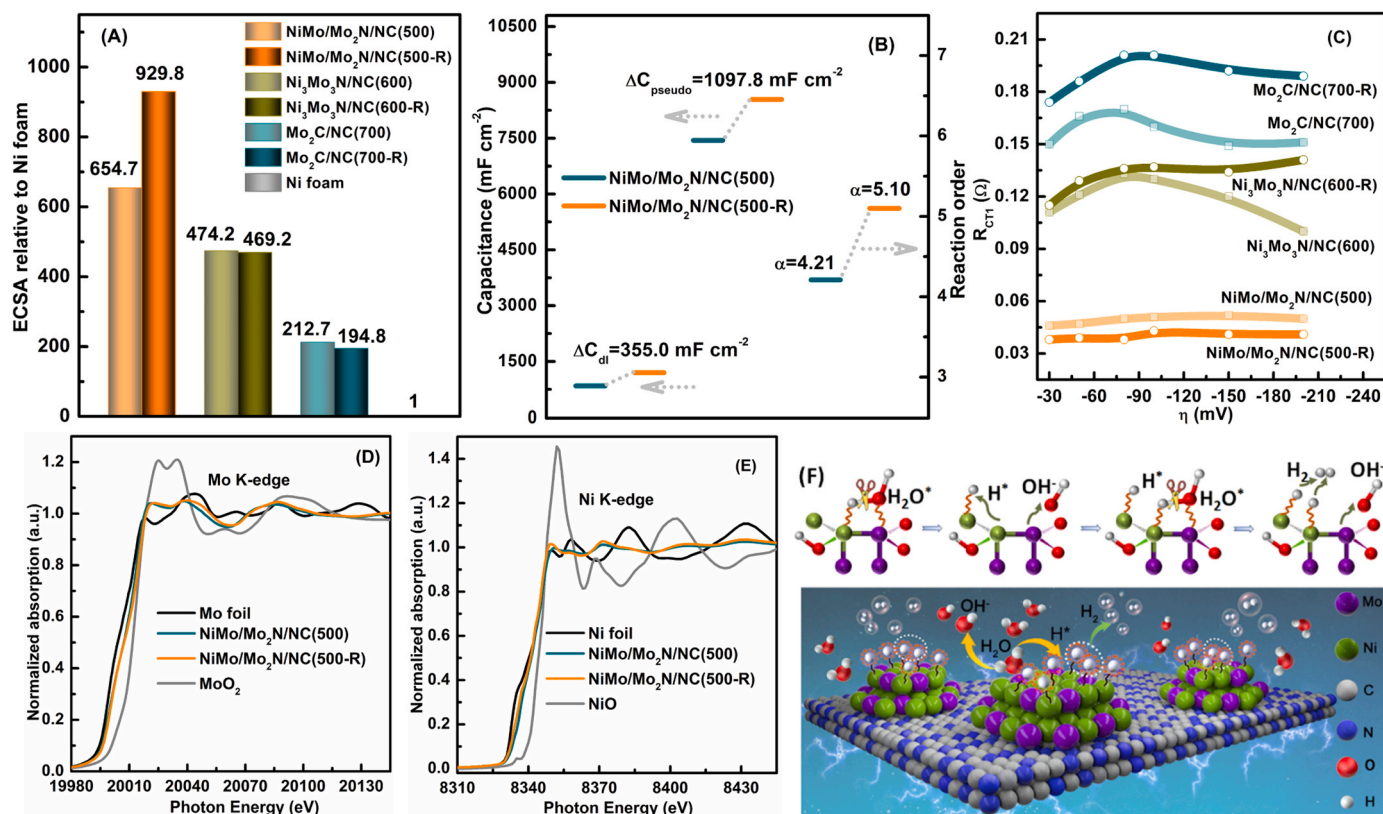


Fig. 4. Insight into catalytic mechanism of CDAEs in alkaline HER. (A) ECSAs relative to Ni foam; (B) Comparison of the stored-charge capacity and reaction order; (C) R_{ct1} as a function of overpotential derived from *operando* EIS fitting results; (D) and (E) Normalized Mo and Ni K-edge XANES spectra; (F) Illustrating typical adsorption/desorption configurations on NiMo/Mo₂N/NC(500-R).

(500-R) (Fig. S25). The mass transfers in HER is related to H^* adsorption, OH^- desorption, hydrogen recombination and water re-adsorption, and dictate the electrocatalytic efficiency under high current densities. The Nyquist plots indicate the near zero-resistance across the nanorod, current collector and electrolyte interfaces owing to the metallic conductivity of NiMo/Mo₂N, and two semicircles that are fitted by Armstrong equivalent electric circuit (Fig. S26). The semicircle in high frequency (R_{ct1}) is related to mass transfers, and the semicircle in low frequency (R_{ct2}) to charge transfer [66]. Typically, R_{ct2} depends on intrinsic activity, decreases monotonically with overpotential (Fig. S27), and cannot elucidate the different activities of catalysts, particularly at large current densities. Among these catalysts, notably, R_{ct1} presents the second smallest value for NiMo/Mo₂N/NC(500), which is further reduced by hydroxylation to the smallest value for NiMo/Mo₂N/NC(500-R) (Fig. 4C). Specifically, their R_{ct1} values are largely independent on overpotentials and current densities. In contrast, the crystallized Ni₃Mo₃N/NC(600) gives larger R_{ct1} , and Mo₂C/NC(700) lacking CDAEs has the largest R_{ct1} . After ESRC, R_{ct1} increases in both Ni₃Mo₃N/NC(600-R) and Mo₂C/NC(700-R), becoming more detrimental to HER kinetics at high overpotentials. The evolutions of R_{ct1} with overpotentials is roughly similar to the dependences of η and $\Delta\eta/\Delta\log|j|$ on current density, indicating the construction of CDAEs is critical to achieve optimal HER kinetics. Clearly, the well-separated CDAEs enable NiMo/Mo₂N/NC(500-R) to have the most efficient mass transfers, ensuring the robust activity even when $j \geq 500 \text{ mA cm}^{-2}$.

The water dissociation and mass transfers are intrinsically linked with the electronic characteristics of CDAEs, as revealed by X-ray absorption near-edge structure (XANES) and extended X-ray absorption fine structure (EXAFS) spectra. Relative to adsorption edge of Mo foil, the Mo K-edge XANES spectra in NiMo/Mo₂N/NC(500) and NiMo/Mo₂N/NC(500-R) shift to high energy, and their closely matched K-edges suggest similar valence state (φ) of 1.28 and 1.32 (Fig. 4D and

S28A). The Ni K-edge of NiMo/Mo₂N/NC(500) is close to that of Ni foil (Fig. 4E), delivering φ of 0.49 (Fig. S28B). After ESRC, interestingly, the absorption edge of NiMo/Mo₂N/NC(500-R) shifts to lower energy, and φ decreases to 0.34, signifying the electron transfer from Mo to Ni atoms. The electron transfer is further evidenced by Fourier-transformed EXAFS in R space and the fitted EXAFS results (Fig. S29 and Table S5). NiMo/Mo₂N/NC(500) exhibits similar coordination shells before and after ESRC. Nevertheless, the elongated Ni-Ni bond around 2.28 Å in R space of NiMo/Mo₂N/NC(500) contracts to 2.21 Å in NiMo/Mo₂N/NC(500-R). This signals that the electronic structures of NiMo/Mo₂N/NC(500-R) are closer to that of Ni foil with Ni-Ni bond of 2.19 Å owing to electron transfer. Moreover, the diminishment of oscillation intensity illustrates the nanostructured NiMo/Mo₂N heterojunctions with reduced periodicity (Fig. S30). Evidently, the electron-deficient Mo species with eligible φ ($1 < \varphi < 2$) expedite water adsorption by capturing oxygen atoms, but not to weaken OH^- desorption. Meanwhile, the electron-rich Ni species convey the electronic properties of Ni foil, favoring the acceptance of hydrogen atoms and hydrogen spillover, and facilitating H_2 release. These observations are accordant with XPS analyses. Compared to NiMo/Mo₂N/NC(500), clearly, the superior catalytic activity of NiMo/Mo₂N/NC(500-R) initiated by ESRC results from the enhanced asymmetrical charge redistributions between Mo and Ni atoms in CDAEs. Hence, the H-OH cleaving and the adsorption/desorption of intermediates can be assigned mainly to the ensemble effect in NiMo/Mo₂N heteronanojunction, resulting from the diatomic charge polarizations in Mo-Ni species, as depicted in Fig. 4F.

3.4. Overall water-splitting performances

For water electrolysis, NiFe-LDH/NiMo/Mo₂N/NC(500) anode was fabricated by electrodeposition of NiFe-layered double hydroxide (NiFe-LDH), with NiMo/Mo₂N/NC(500) serving as array template. SEM

images demonstrate that the array architecture is preserved, and NiFe-LDH nanosheets epitaxially grow along NiMo/Mo₂N/NC nanorods to present the petal-like arrangements (Fig. 5A and Fig. S31). XRD pattern verifies the successful deposition of NiFe-LDH on NiMo/Mo₂N/NC500 during electrochemical-treatment (Fig. S32). The electrocatalysis of NiFe-LDH/NiMo/Mo₂N/NC(500) in alkaline OER was evaluated by LSVs in O₂-saturated 1 M KOH, and the overpotentials of 228 and 300 mV respectively deliver current densities of 100 and 500 mA cm⁻². These results are superior to those of nickel foam-supported NiFe-LDH and significantly outperform the benchmark of nickel foam-supported RuO₂ (Fig. 5B). The enhanced catalytic activity in OER profit from the array template of NiMo/Mo₂N/NC(500) guiding NiFe-LDH growth.

In light of the impressive HER and OER performances, the water-alkali electrolyzers were assembled using NiFe-LDH/NiMo/Mo₂N/NC(500) or NiMo/Mo₂N/NC(500-R) as the anode, and NiMo/Mo₂N/NC(500-R), NiMo/Mo₂N/NC(500) or NiFe-LDH/NiMo/Mo₂N/NC(500) as the cathode, and 1 M KOH solution as electrolyte, to estimate the practical overall water splitting. The polarization curves of overall water-splitting reveal that the NiFe-LDH/NiMo/Mo₂N/NC(500)∥NiMo/Mo₂N/NC(500-R) electrolyzer exhibits an ultralow cell voltage of 1.530 and 1.607 V respectively at 100 and 500 mA cm⁻², outperforming the other configurations (Fig. 5C). These results underscore the combination of catalysts with high HER and OER activities to achieve the optimal overall-water-splitting efficiency in the NiFe-LDH/NiMo/Mo₂N/NC(500)∥NiMo/Mo₂N/NC(500-R) asymmetric electrolyzer. The

operational stability of NiFe-LDH-NiMo/Mo₂N/NC(500)∥NiMo/Mo₂N/NC(500-R) electrolyzer was evaluated by chronoamperometry at 500 mA cm⁻² and cell voltage of 1.607 V (Fig. 5D). After 200 h of operation, the electrolyzer retains remarkable overall water splitting performance with a voltage drop of 15 mV. The catalytic activity and stability outshine most previously reported water electrolyzers in alkaline media (Table S6).

4. Conclusions

The fully-exposed NiMo/Mo₂N heteronanojunctions in nitrogen-rich IL-derived carbons imparts NiMo/Mo₂N/NC(500-R) array with enormous ECSA, specifically up to 929.8 times larger than that of nickel foam. The ensemble effect from the densely packed NiMo/Mo₂N heteronanojunctions induces the diatomic charge polarizations that can be enhanced by the surface hydroxylation via ESRC. The superior catalytic activity of NiMo/Mo₂N/NC(500-R) in HER results from abundant available CDAEs, heavy charge accumulation in pre-reaction, and rapid mass transfers to refresh active sites vigorously. Hence, the concerted catalysis on CDAEs fulfills large-current alkaline HER, and proceeds with synchronous dual-mechanism: one is oxygen capture of H₂O, and OH⁻ desorption on the electron-deficient Mo species, the other is H⁺ reception/spillover, and H₂ release on the electron-rich Ni species. It is demonstrated that NiMo/Mo₂N/NC(500-R) achieves ultra-low overpotentials of 5.8, 117.0 and 200.6 mV, as well as Δη/Δlog|j| of 7.0, 99.0

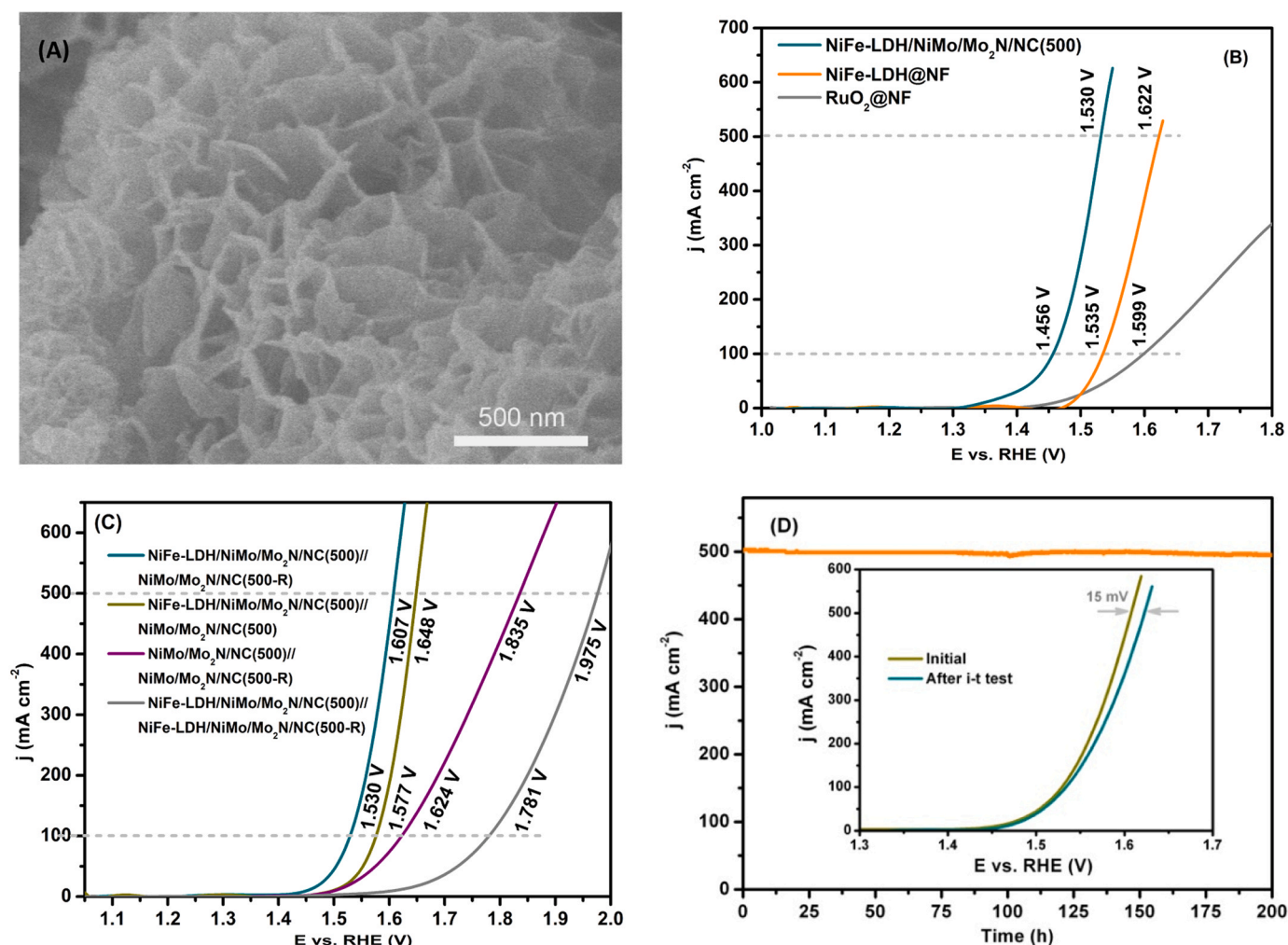


Fig. 5. Overall water electrolysis. (A) SEM image of NiFe-LDH/NiMo/Mo₂N/NC(500); (B) Polarization curves of OER at a scan rate of 2 mV s⁻¹ in O₂-saturated 1 M KOH aqueous solution; (C) Polarization curves of overall water-splitting at a scan rate of 2 mV s⁻¹ in 1 M KOH aqueous solution; (D) Long-term durability of NiFe-LDH/NiMo/Mo₂N/NC(500)∥NiMo/Mo₂N/NC(500-R) in overall water-splitting, inset: the polarization curves before and after 200 h test.

and 153.1 mV dec⁻¹ at 10, 500 and 1000 mA cm⁻², respectively, surpassing the performances of Pt-based electrocatalysts. Although the array's nanorods are constructed by NiMo and Mo₂N crystallites, NiMo/Mo₂N/NC(500-R) can withstand the harsh operation conditions of HER owing to the bonding of nitrogen-rich NC skeleton with the crystallites, and shows only a minor overpotential increase of 123 mV after continuous operation for 1000 h at 1000 mA cm⁻². As water-alkali electrolyzer is assembled with NiFe-LDH-NiMo/Mo₂N/NC(500) anode, NiMo/Mo₂N/NC(500-R) cathode represents excellent overall water-splitting performances with a cell voltage of only 1.530 V at 100 mA cm⁻². This study provides generalizable models for designing CDAE catalysts with regulatable surface charge-polarizations using different metallic heterojunctions and various nonvolatile ionic liquids, addressing commercialization requirements for electrocatalysts with high activity and durability, not just for HER.

CRediT authorship contribution statement

Huanli Jia: Conceptualization, Methodology, Investigation, Data curation, Formal analysis, Writing – original draft. **Fangfang Yan:** Investigation, Data curation. **Ze Li:** Formal analysis, Data curation. **Haiyan Wang:** Writing – review & editing, Software, Funding acquisition, Supervision. **Hucheng Zhang:** Conceptualization, Writing – review & editing, Funding acquisition, Supervision, Project administration. **Jianji Wang:** Writing – review & editing, Supervision, Project administration.

Declaration of Competing Interest

The authors declare that they have no known competing financial interests or personal relationships that could have appeared to influence the work reported in this paper.

Data Availability

No data was used for the research described in the article.

Acknowledgments

This work is supported by the National Natural Science Foundation of China (21573059 and 22208088).

Appendix A. Supporting information

Supplementary data associated with this article can be found in the online version at [doi:10.1016/j.apcatb.2023.123362](https://doi.org/10.1016/j.apcatb.2023.123362).

References

- S. Chu, A. Majumdar, Opportunities and challenges for a sustainable energy future, *Nature* 488 (2012) 294–303, <https://doi.org/10.1038/nature11475>.
- P.D. Luna, C. Hahn, D. Higgins, S.A. Jaffer, T.F. Jaramillo, E.H. Sargent, What would it take for renewably powered electrosynthesis to displace petrochemical processes? *Science* 364 (2019) 350, <https://doi.org/10.1126/science.aav3506>. (<https://www.science.org/doi/epdf/>).
- Z.W. Seh, J. Kibsgaard, C.F. Dickens, I. Chorkendorff, T.F. Jaramillo, Combining theory and experiment in electro-catalysis: insights into materials design, *Science* 355 (2017) eaad4998, <https://www.science.org/doi/10.1126/science.aad4998>.
- Z.Y. Yu, Y. Duan, X.Y. Feng, X.X. Yu, M.R. Gao, S.H. Yu, Clean and affordable hydrogen fuel from alkaline water splitting: past, recent progress, and future prospects, *Adv. Mater.* 33 (2021), 2007100, <https://doi.org/10.1002/adma.202007100>.
- H.M. Sun, Z.H. Yan, F.M. Liu, W.C. Xu, F.Y. Cheng, J. Chen, Self-supported transition-metal-based electrocatalysts for hydrogen and oxygen evolution, *Adv. Mater.* 32 (2020), 1806326, <https://doi.org/10.1002/adma.201806326>.
- Y.L. Zhu, Q. Lin, Y.J. Zhong, H.A. Tahini, Z.P. Shao, H.T. Wang, Metal oxide-based materials as an emerging family of hydrogen evolution electrocatalysts, *Energy Environ. Sci.* 13 (2020) 3361–3392, <https://doi.org/10.1039/D0EE02485F>.
- Z.W. Zhuang, Y. Wang, C.Q. Xu, S.J. Liu, C. Chen, Q. Peng, Z.B. Zhuang, H. Xiao, Y. Pan, S.Q. Lu, et al., Three-dimensional open nano-netcage electrocatalysts for efficient pH-universal overall water splitting, *Nat. Commun.* 10 (2019) 4875, <https://doi.org/10.1038/s41467-019-12885-0>.
- Q. Liu, S.J. Sun, L.C. Zhang, Y.S. Luo, Q. Yang, K. Dong, X.D. Fang, D.D. Zheng, A. Alshehri, X.P. Sun, N. O-doped carbon foam as metal-free electrocatalyst for efficient hydrogen production from seawater, *Nano Res.* 15 (2022) 8922–8927, <https://doi.org/10.1007/s12274-022-4869-2>.
- J. Kim, H. Kim, W.J. Lee, B. Ruqia, H. Baik, H.S. Oh, S.M. Paek, H.K. Lim, C. H. Choi, S.I. Choi, Theoretical and experimental understanding of hydrogen evolution reaction kinetics in alkaline electrolytes with Pt-based core-shell nanocrystals, *J. Am. Chem. Soc.* 141 (2019) 18256–18263, <https://doi.org/10.1021/jacs.9b09229>.
- Y. Zheng, Y. Jiao, A. Vasileff, S.Z. Qiao, The hydrogen evolution reaction in alkaline solution: from theory, single crystal models, to practical electrocatalysts, *Angew. Chem. Int. Ed.* 57 (2018) 7568–7579, <https://doi.org/10.1002/anie.201710556>.
- L. Ouyang, X. He, Y.T. Sun, L.C. Zhang, D.L. Zhao, S.J. Sun, Y.S. Luo, D.D. Zheng, A. M. Asiri, Q. Liu, J.X. Zhao, X.P. Sun, RuO₂ nanoparticle-decorated TiO₂ nanobelt array as a highly efficient electrocatalyst for the hydrogen evolution reaction at all pH values, *Inorg. Chem. Front.* 9 (2022) 6602–6607, <https://doi.org/10.1039/D2QI02205B>.
- X.D. Fang, X.G. Wang, L. Ouyang, L.C. Zhang, S.J. Sun, Y.M. Liang, Y.S. Luo, D. D. Zheng, T.R. Kang, Q. Liu, F. Huo, X.P. Sun, Amorphous Co-Mo-B film: a high-active electrocatalyst for hydrogen generation in alkaline seawater, *Molecules* 27 (2022) 7617, <https://doi.org/10.3390/molecules27217617>.
- J. Yin, J. Jin, H.H. Lin, Z.Y. Yin, J.Y. Li, M. Lu, L.C. Guo, P.X. Xi, Y. Tang, C.H. Yan, Optimized metal chalcogenides for boosting water splitting, *Adv. Sci.* 7 (2020), 1903070, <https://doi.org/10.1002/adv.201903070>.
- J.J. Lu, S.B. Yin, P.K. Shen, Carbon-encapsulated electrocatalysts for the hydrogen evolution reaction, *Electrochem. Energy Rev.* 2 (2019) 105–127, <https://doi.org/10.1007/s41918-018-0025-9>.
- L.X. Lin, P. Sherrell, Y.Q. Liu, W. Lei, S.W. Zhang, H.J. Zhang, G.G. Wallace, J. Chen, Engineered 2D transition metal dichalcogenides—a vision of viable hydrogen evolution reaction catalysis, *Adv. Energy Mater.* 10 (2020), 1903870, <https://doi.org/10.1002/aenm.201903870>.
- J. Wang, W.H. Fang, Y. Hu, Y.H. Zhang, J.Q. Dang, Y. Wu, B.Z. Chen, H. Zhao, Z. X. Li, Single atom Ru doping 2H-MoS₂ as highly efficient hydrogen evolution reaction electrocatalyst in a wide pH range, *Appl. Catal. B* 298 (2021), 120490, <https://doi.org/10.1016/j.apcatb.2021.120490>.
- K.X. Zhang, X. Liang, L.N. Wang, K. Sun, Y.N. Wang, Z.B. Xie, Q.N. Wu, X.Y. Bai, M. S. Hamdy, H. Chen, X.X. Zou, Status and perspectives of key materials for PEM electrolyzer, *Nano Res. Energy* 1 (2022), e9120032, <https://doi.org/10.26599/NRE.2022.9120032>.
- L.C. Zhang, L. Li, J. Liang, X.Y. Fan, X. He, J. Chen, J. Li, Z.X. Li, Z.W. Cai, S.J. Sun, D.D. Zheng, Y.S. Luo, H. Yan, Q. Liu, A.A. Alshehri, X.D. Guo, X.P. Sun, B.W. Ying, Highly efficient and stable oxygen evolution from seawater enabled by a hierarchical NiMoS_x microcolumn@NiFe-layered double hydroxide nanosheet array, *Inorg. Chem. Front.* 10 (2023) 2766–2775, <https://doi.org/10.1039/D3QI00341H>.
- S.L. Zhang, F.X. Lu, Z.P. Wu, D.Y. Luan, X.W. Lou, Engineering platinum-cobalt nano-alloys in porous nitrogen-doped carbon nanotubes for highly efficient electrocatalytic hydrogen evolution, *Angew. Chem. Int. Ed.* 60 (2021) 19068–19073, <https://doi.org/10.1002/anie.202106547>.
- P. Sabhapathy, I. Shown, A. Sabbah, P. Raghunath, J.L. Chen, W.F. Chen, M.C. Lin, K.H. Chen, L.C. Chen, Electronic structure modulation of isolated Co-N₄ electrocatalyst by sulfur for improved pH-universal hydrogen evolution reaction, *Nano Energy* 80 (2021), 105544, <https://doi.org/10.1016/j.nanoen.2020.105544>.
- N. Mahmood, Y.D. Yao, J.W. Zhang, L. Pan, X.W. Zhang, J.J. Zou, Electrocatalysts for hydrogen evolution in alkaline electrolytes: mechanisms, challenges, and prospective solutions, *Adv. Sci.* 5 (2018), 1700464, <https://doi.org/10.1002/adv.201700464>.
- P.M. Bodhankar, P.B. Sarawade, P. Kumar, A. Vinu, A.P. Kulkarni, C.D. Lokhande, D.S. Dhawale, Nanostructured metal phosphide based catalysts for electrochemical water splitting: a review, *Small* 18 (2022), 2107572, <https://doi.org/10.1002/smll.202107572>.
- J.Q. Zhang, X. Shang, H. Ren, J.Q. Chi, H. Fu, B. Dong, C.G. Liu, Y.M. Cha, Modulation of inverse spinel Fe₃O₄ by phosphorus doping as an industrially promising electrocatalyst for hydrogen evolution, *Adv. Mater.* 31 (2019), 1905107, <https://doi.org/10.1002/adma.201905107>.
- B. Zhang, L.S. Zhang, Q.Y. Tan, J.S. Wang, J. Liu, H.Z. Wan, L. Miao, J.J. Jiang, Simultaneous interfacial chemistry and inner Helmholtz plane regulating for superior alkaline hydrogen evolution, *Energy Environ. Sci.* 13 (2020) 3007–3013, <https://doi.org/10.1039/D0EE02020F>.
- Y. Cao, T. Wang, X. Li, L.C. Zhang, Y.L. Luo, F. Zhang, A.M. Asiri, J.M. Hu, Q. Liu, X.P. Sun, A hierarchical CuO@NiCo layered double hydroxide core-shell nanoarray as an efficient electrocatalyst for the oxygen evolution reaction, *Inorg. Chem. Front.* 8 (2021) 3049–3054, <https://doi.org/10.1039/D1QI00124H>.
- L. Deng, F. Hu, M.Y. Ma, S.C. Huang, Y.X. Xiong, H.Y. Chen, L.L. Li, S.G. Peng, Electronic modulation caused by interfacial Ni-O-M (M = Ru, Ir, Pd) bonding for accelerating hydrogen evolution kinetics, *Angew. Chem. Int. Ed.* 60 (2021) 22276–22282, <https://doi.org/10.1002/anie.202110374>.
- J. Chen, L.C. Zhang, J. Li, X. He, Y.Y. Zheng, S.J. Sun, X.D. Fang, D.D. Zheng, Y. S. Luo, Y. Wang, J. Zhang, L.S. Xie, Z.W. Cai, Y.T. Sun, A.A. Alshehri, Q.Q. Kong, C. W. Tang, X.P. Sun, High-efficiency overall alkaline seawater splitting: using a nickel-iron sulfide nanosheet as a bifunctional electrocatalyst, *J. Mater. Chem. A* 11 (2023) 1116–1122, <https://doi.org/10.1039/D2TA08568B>.

- [28] L. Wang, J.H. Cao, C.J. Lei, Q.Z. Dai, B. Yang, Z.G. Li, X.W. Zhang, C. Yuan, L. C. Lei, Y. Hou, Strongly coupled 3D N-Doped MoO₂/Ni₃S₂ hybrid for high current density hydrogen evolution electrocatalysis and biomass upgrading, *ACS Appl. Mater. Interfaces* 11 (2019) 27743–27750, <https://doi.org/10.1021/acsami.9b06502>.
- [29] X. Zhang, Z.M. Luo, P. Yu, Y.Q. Cai, Y.H. Du, D.X. Wu, S. Gao, C.L. Tan, Z. Li, M. Q. Ren, et al., Lithiation-induced amorphization of Pd₃P₂S₈ for highly efficient hydrogen evolution, *Nat. Catal.* 1 (2018) 460–468, <https://doi.org/10.1038/s41929-018-0072-y>.
- [30] S. Anantharaj, H. Sugime, S. Noda, Surface amorphized nickel hydroxy sulphide for efficient hydrogen evolution reaction in alkaline medium, *Chem. Eng. J.* 408 (2021), 127275, <https://doi.org/10.1016/j.cej.2020.127275>.
- [31] C.X. Niu, H. Song, Y.Z. Chang, W.J. Hou, Y.P. Li, Y.M. Zhao, G.Y. Han, Amorphous MoS_x electro-synthesized in alkaline electrolyte for superior hydrogen evolution, *J. Alloy. Compd.* 900 (2022), 163509, <https://doi.org/10.1016/j.jallcom.2021.163509>.
- [32] Y. Zhou, W. Hao, X.X. Zhao, J.D. Zhou, H.M. Yu, B. Lin, Z. Liu, S.J. Pennycook, S. Z. Li, H.J. Fan, Electronegativity-Induced charge balancing to boost stability and activity of amorphous electrocatalyst, *Adv. Mater.* 34 (2022), 2100537, <https://doi.org/10.1002/adma.202100537>.
- [33] F.D. Ning, J.Q. Qin, X. Dan, S.F. Pan, C. Bai, M. Shen, Y.L. Li, X.W. Fu, S. Zhou, Y. B. Shen, W. Feng, Y.C. Zou, Y. Cui, Y.J. Song, X.C. Zhou, Nanosized proton conductor array with high specific surface area improves fuel cell performance at low Pt loading, *ACS Nano* 17 (2023) 9487–9500, <https://doi.org/10.1021/acsnano.3c01690>.
- [34] Y.T. Luo, Z.Y. Zhang, M. Chhowalla, B.L. Liu, Recent advances in design of electrocatalysts for high-current-density water splitting, *Adv. Mater.* 34 (2022), 2108133, <https://doi.org/10.1002/adma.202108133>.
- [35] M.M. Lao, P. Li, Y.Z. Jiang, H.G. Pan, S.X. Dou, W.P. Sun, From fundamentals and theories to heterostructured electrocatalyst design: an in-depth understanding of alkaline hydrogen evolution reaction, *Nano Energy* 98 (2022), 107231, <https://doi.org/10.1016/j.nanoen.2022.107231>.
- [36] N. Vöhrler, R. Rao, L. Giordano, Y. Shao-Horn, U. Aschauer, Implications of nonelectrochemical reaction steps on the oxygen evolution reaction: oxygen dimer formation on perovskite oxide and oxynitride surfaces, *ACS Catal.* 12 (2022) 1433–1442, <https://doi.org/10.1021/acscatal.1c03308>.
- [37] H.H. Pham, M.J. Cheng, H. Frei, L.W. Wang, Surface proton hopping and fast-kinetics pathway of water oxidation on Co₃O₄ (001) surface, *ACS Catal.* 6 (2016) 5610–5617, <https://doi.org/10.1021/acscatal.6b00713>.
- [38] J. k Li, A. Alsaadairi, Z.F. Ma, S. Mukerjee, Q.Y. Jia, Asymmetric volcano trend in oxygen reduction activity of Pt and non-Pt catalysts: in situ identification of the site-blocking effect, 1384–138, *J. Am. Chem. Soc.* 139 (2017), <https://doi.org/10.1021/jacs.6b11072>.
- [39] R. Subbaraman, D. Tripkovic, D. Strmcnik, K.C. Chang, M. Uchiumura, A. P. Paulikas, V. Stamenkovic, N.M. Markovic, Enhancing hydrogen evolution activity in water splitting by tailoring Li⁺-Ni(OH)₂-Pt interfaces, *Science* 334 (2011) 1256–1260, <https://www.science.org/doi/10.1126/science.1211934>.
- [40] C. Panda, P.W. Menezes, S.L. Yao, J. Schmidt, C. Walter, J.N. Hausmann, M. Driess, Boosting electrocatalytic hydrogen evolution activity with a NiPt₃@NiS heterostructure evolved from a molecular nickel-platinum precursor, *J. Am. Chem. Soc.* 141 (2019) 13306–13310, <https://doi.org/10.1021/jacs.9b06530>.
- [41] Y. Liu, J.H. Wu, Y.C. Zhang, X. Jin, J.M. Li, X.K. Xi, Y. Deng, S.H. Jiao, Z.W. Lei, X. Y. Li, R.G. Cao, Ensemble effect of ruthenium single-atom and nanoparticle catalysts for efficient hydrogen evolution in neutral media, *ACS Appl. Mater. Interfaces* 15 (2023) 14240–14249, <https://doi.org/10.1021/acsami.2c20863>.
- [42] J. Zhang, T. Wang, P. Liu, Z.Q. Liao, S.H. Liu, X.D. Zhuang, M.W. Chen, E. Zschech, X.L. Feng, Efficient hydrogen production on MoNi₄ electrocatalysts with fast water dissociation kinetics, *Nat. Commun.* 8 (2017) 15437, <https://doi.org/10.1038/ncomms15437>.
- [43] H.C. Zhang, M.M. Wang, J. Zhao, S.T. Han, H.X. Cheng, J.J. Wang, Electrochemical recognition of alkylimidazolium-mediated ultrafast charge transfer on graphene surfaces, *Chem. Commun.* 54 (2018) 666, <https://doi.org/10.1039/C7CC08138C>.
- [44] D. Liu, H.Q. Ai, J.L. Li, M.L. Fang, M.P. Chen, D. Liu, X.Y. Du, P.F. Zhou, F.F. Li, K. H. Lo, et al., Surface reconstruction and phase transition on vanadium-cobalt-iron trimetal nitrides to form active oxyhydroxide for enhanced electrocatalytic water oxidation, *Adv. Energy Mater.* 10 (2020), 2002464, <https://doi.org/10.1021/acsami.2c20863>.
- [45] Y.T. Luo, Z.Y. Zhang, F.N. Yang, J. Li, Z.B. Liu, W.C. Ren, S. Zhang, B.L. Liu, Stabilized hydroxide-mediated nickel-based electrocatalysts for high-current-density hydrogen evolution in alkaline media, *Energy Environ. Sci.* 14 (2021) 4610–4619, <https://doi.org/10.1039/D1EE01487K>.
- [46] Y.Y. Chen, Y. Zhang, X. Zhang, T. Tang, H. Luo, S. Niu, Z.H. Dai, L.J. Wan, J.S. Hu, Self-templated fabrication of MoNi₄/MoO_{3-x} nanoarrays with dual active components for highly efficient hydrogen evolution, *Adv. Mater.* 29 (2017), 1703311, <https://doi.org/10.1002/adma.201703311>.
- [47] M.J. Xiao, B. Ma, Z.Q. Zhang, Q. Xiao, X.Y. Li, Z.T. Zhang, Q. Wang, Y. Peng, H. L. Zhang, Carbon nano-onion encapsulated cobalt nanoparticles for oxygen reduction and lithium-ion batteries, *J. Mater. Chem. A* 9 (2021) 7227, <https://doi.org/10.1039/D0TA12504K>.
- [48] Z.X. Xu, S. Jin, M.H. Seo, X.L. Wang, Hierarchical Ni-Mo₂C/N-doped carbon Mott-Schottky array for water electrolysis, *Appl. Catal. B* 292 (2021), 120168, <https://doi.org/10.1016/j.apcatb.2021.120168>.
- [49] Y.L. Qiu, Z.Q. Liu, A.W. Sun, X.Y. Zhang, X.Q. Ji, J.Q. Liu, Electrochemical in situ self-healing of porous nanosheets based on the phase reconstruction of carbonate hydroxide to layered double hydroxides with unsaturated coordination metal sites for high-performance water oxidation, *ACS Sustain. Chem. Eng.* 10 (2022) 16417–16426, <https://doi.org/10.1021/acssuschemeng.2c05705>.
- [50] M.W. Louie, A.T. Bell, An investigation of thin-film Ni-Fe oxide catalysts for the electrochemical evolution of oxygen, *J. Am. Chem. Soc.* 135 (2013) 12329–12337, <https://doi.org/10.1021/ja405351s>.
- [51] N. Zhang, Y. Hu, L. An, Q.Y. Li, J. Yin, J.Y. Li, R. Yang, M. Lu, S. Zhang, P.X. Xi, C. H. Yan, Surface activation and Ni-S stabilization in NiO/NiS₂ for efficient oxygen evolution reaction, *Angew. Chem. Int. Ed.* 61 (2022), e20220721, <https://doi.org/10.1002/anie.202207217>.
- [52] L. Yu, Q. Zhu, S.W. Song, B. McElhenry, D.Z. Wang, C.Z. Wu, Z.J. Qin, J.M. Bao, Y. Yu, S. Chen, Z.F. Ren, Non-noble metal-nitride based electrocatalysts for high-performance alkaline seawater electrolysis, *Nat. Commun.* 10 (2019) 5106, <https://doi.org/10.1038/s41467-019-13092-7>.
- [53] C.T. Dinh, A. Jain, P.P.G. de Arquer, P.D. Luna, J. Li, N. Wang, X.L. Zheng, J. Cai, B. Z. Gregory, B.Z. Voznyy, et al., Multi-site electrocatalysts for hydrogen evolution in neutral media by destabilization of water molecules, *Nat. Energy* 4 (2019) 107–114, <https://doi.org/10.1038/s41560-018-0296-8>.
- [54] Z. Zhou, Z.W. Yuan, S. Li, J.S. Chen, Y.Q. Wang, Q.W. Huang, C. Wang, H. E. Karahan, G. Henkelman, et al., Big to Small: Ultrafine Mo₂C particles derived from giant polyoxomolybdate clusters for hydrogen evolution reaction, *Small* 15 (2019), 1900358, <https://doi.org/10.1002/smll.201900358>.
- [55] Y.K. Chen, J.Y. Yu, J. Jia, F. Liu, Y.W. Zhang, G.W. Xiong, R.T. Zhang, R.Q. Yang, D.H. Sun, H. Liu, W.J. Zhou, Metallic Ni₃Mo₃N porous microrods with abundant catalytic sites as efficient electrocatalyst for large current density and superstability of hydrogen evolution reaction and water splitting (<https://doi.org/>), *Appl. Catal. B* 272 (2020), 118956, <https://doi.org/10.1016/j.apcatb.2020.118956>.
- [56] Y. Luo, L. Tang, U. Khan, Q.M. Yu, H.M. Cheng, X.L. Zou, B.L. Liu, Morphology and surface chemistry engineering toward pH-universal catalysts for hydrogen evolution at high current density, *Nat. Commun.* 10 (2019) 269, <https://doi.org/10.1038/s41467-018-07792-9>.
- [57] D.B. Liu, X.Y. Li, S.M. Chen, H. Yan, C.D. Wang, C.Q. Wu, Y.A. Haleem, S. Duan, J. L. Lu, B.H. Ge, P.M. Ajayan, Y. Luo, J. Jiang, L. Song, Atomically dispersed platinum supported on curved carbon supports for efficient electrocatalytic hydrogen evolution, *Nat. Energy* 4 (2019) 512–518, <https://doi.org/10.1038/s41560-019-0402-6>.
- [58] S. Fang, X.R. Zh u, X.K. Liu, J. Gu, W. Liu, D.H. Wang, W. Zhang, Y. Lin, J.L. Lu, S. Q. Wei, Y.F. Li, T. Yao, Uncovering near-free platinum single-atom dynamics during electrochemical hydrogen evolution reaction, *Nat. Commun.* 11 (2020) 1029, <https://doi.org/10.1038/s41467-020-14848-2>.
- [59] J.Q. Zhang, Y.F. Zhao, X. Guo, C. Chen, C.L. Dong, R.S. Liu, C.P. Han, Y.D. Li, Y. Gogotsi, G.X. Wang, Single platinum atoms immobilized on an MXene as an efficient catalyst for the hydrogen evolution reaction, *Nat. Catal.* 1 (2018) 985–992, <https://doi.org/10.1038/s41929-018-0195-1>.
- [60] C.Y. Li, Z.J. Wang, M.D. Liu, E.Z. Wang, B.L. Wang, L.L. Xu, K.L. Jiang, S.S. Fan, Y. H. Sun, J. Li, K. Liu, Ultrafast self-heating synthesis of robust heterogeneous nanocarbons for high current density hydrogen evolution reaction, *Nat. Commun.* 13 (2022) 3338, <https://doi.org/10.1038/s41467-022-31077-x>.
- [61] Z.Y. Wang, J.Y. Chen, E.H. Song, N. Wang, J.C. Dong, X. Zhang, P.M. Ajayan, W. Yao, C.F. Wang, J.J. Liu, J.F. Shen, M.X. Ye, Manipulation on active electronic states of metastable phase β-NiMoO₄ for large current density hydrogen evolution, *Nat. Commun.* 12 (2021) 5960, <https://doi.org/10.1038/s41467-021-26256-1>.
- [62] S. Gao, Y. Li, X.C. Jiao, Y.F. Sun, Q.Q. Luo, W.H. Zhang, D.Q. Li, J.L. Yang, Y. Xie, Partially oxidized atomic cobalt layers for carbon dioxide electroreduction to liquid fuel, *Nature* 529 (2016) 68, <https://doi.org/10.1038/nature16455>.
- [63] D.W. Wang, Q. Li, C. Han, Q.Q. Lu, Z.C. Xing, X.R. Yang, Atomic and electronic modulation of self-supported nickel-vanadium layered double hydroxide to accelerate water splitting kinetics, *Nat. Commun.* 10 (2019) 3899, <https://doi.org/10.1038/s41467-019-11765-x>.
- [64] H.N. Nong, L.J. Falling, A. Bergmann, M. Klingenhof, H.P. Tran, C. Spöri, R. Mom, J. Timoshenko, G. Zichittella, A. Knop-Gericke, et al., Key role of chemistry versus bias in electrocatalytic oxygen evolution, *Nature* 587 (2020) 408–413, <https://doi.org/10.1038/s41586-020-2908-2>.
- [65] Y.W. Dai, J. Yu, J. Wang, Z.P. Shao, D.Q. Guan, Y.C. Huang, M. Ni, Bridging the charge accumulation and high reaction order for high-rate oxygen evolution and long stable Zn-Air batteries, *Adv. Funct. Mater.* 32 (2022), 2111989, <https://doi.org/10.1002/adfm.202111989>.
- [66] L.F. Shen, B.A. Lu, Y.Y. Li, J. Liu, Z.C. Huang-Fu, H. Peng, J.Y. Ye, X.M. Qu, J. M. Zhang, G. Li, et al., Interfacial structure of water as a new descriptor of the hydrogen evolution reaction, *Angew. Chem. Int. Ed.* 59 (2020) 22397–22402, <https://doi.org/10.1002/anie.202007567>.